

ARTICLE

<https://doi.org/10.1038/s42005-019-0190-0>

OPEN

# Light emission from the layered metal 2H-TaSe<sub>2</sub> and its potential applications

Mehak Mahajan<sup>1,3</sup>, Sangeeth Kallatt<sup>1,3</sup>, Medha Dandu <sup>1</sup>, Naresh Sharma<sup>2</sup>, Shilpi Gupta<sup>2</sup> & Kausik Majumdar <sup>1</sup>

Conventional metals, in general, do not exhibit strong photoluminescence. 2H-TaSe<sub>2</sub> is a layered transition metal dichalcogenide that possesses metallic property with charge density wave characteristics. Here we show that 2H-TaSe<sub>2</sub> exhibits a surprisingly strong optical absorption and photoluminescence resulting from inter-band transitions. We use this perfect combination of electrical and optical properties in several optoelectronic applications. We show a sevenfold enhancement in the photoluminescence intensity of otherwise weakly luminescent multi-layer MoS<sub>2</sub> through non-radiative resonant energy transfer from TaSe<sub>2</sub> transition dipoles. Using a combination of scanning photocurrent and time-resolved photoluminescence measurements, we also show that the hot electrons generated by light absorption in TaSe<sub>2</sub> have a rather long lifetime unlike conventional metals, making TaSe<sub>2</sub> an excellent hot electron injector. Finally, we show a vertical TaSe<sub>2</sub>/MoS<sub>2</sub>/graphene photodetector demonstrating a responsivity of >10 AW<sup>-1</sup> at 0.1 MHz—one of the fastest reported photodetectors using MoS<sub>2</sub>.

<sup>1</sup>Department of Electrical Communication Engineering, Indian Institute of Science, Bangalore 560012, India. <sup>2</sup>Department of Electrical Engineering, Indian Institute of Technology Kanpur, Kanpur 208016, India. <sup>3</sup>These authors contributed equally: Mehak Mahajan, Sangeeth Kallatt. Correspondence and requests for materials should be addressed to K.M. (email: [kausikm@iisc.ac.in](mailto:kausikm@iisc.ac.in))

Adding new functionalities to devices is one of the important achievements of nano-materials and their heterojunctions. To this end, semiconducting two-dimensional (2D) transition metal dichalcogenides (TMDCs) have been extensively investigated for a plethora of nanoelectronic and optoelectronic applications<sup>1–3</sup>. In general, obtaining a low resistance electrical contact without destroying the high quality of ultra-thin 2D active layers remains an outstanding challenge for 2D materials. Recently, vertical electronic and optoelectronic devices<sup>1,4–6</sup> using layered materials are becoming increasingly popular as they exploit carrier transport through these nanometer-thick active layers—something that is difficult to achieve in a lithography limited conventional planar structure. Maintaining the pristine nature of the layers underneath the contact becomes even more crucial in the context of these vertical devices where the contact physically sits right on top of the active layers.

In this context, metallic TMDCs would be an ideal choice for contact material. However, metallic TMDCs remain a less explored class of materials. 2H-TaSe<sub>2</sub> is one such layered TMDC that shows metallic properties<sup>7–10</sup> and would be promising as a contact material for nanoelectronic devices. 2H-TaSe<sub>2</sub> exhibits simultaneously strong electron–phonon coupling and spin-orbit coupling<sup>11</sup>, which play a crucial role in charge density wave (CDW) driven transport properties. It exhibits highest CDW transition temperature among TMDCs exhibiting 2H symmetry. The resulting bandstructure shows a narrow band around Fermi energy with uniquely structured Fermi surfaces. Interestingly, there is a large gap above and below the bands around the Fermi energy<sup>12–15</sup> in the normal metal phase and is expected to exhibit interesting optical properties, which remain largely unexplored. The perfect combination of excellent electrical transport and optical properties, coupled with the possibility of wafer-scale growth<sup>16</sup>, makes 2H-TaSe<sub>2</sub> a unique material for flexible, “all-2D” optoelectronic applications.

Motivated by this, in this work, we explore 2H-TaSe<sub>2</sub> as a promising multi-purpose optoelectronic material. We show that this material exhibits strong optical absorption and photoluminescence (PL), while maintaining metallic conductivity behavior. These properties have been explored here to demonstrate versatile device applications of 2H-TaSe<sub>2</sub>, for example, (1) as a donor layer for non-radiative resonant energy transfer (NRET)<sup>17–20</sup> to other material, (2) as an efficient hot electron injector, (3) as a contact material for planar and vertical devices, and finally (4) as a dual-purpose layer, namely as light absorber as well as photo-carrier collector, in a sensitive, high speed vertical photodetector.

## Results

We obtain TaSe<sub>2</sub> flakes on Si substrate covered with thermally grown 285-nm SiO<sub>2</sub> using micromechanical exfoliation from bulk crystals (procured from 2D Semiconductors). The bulk crystals are characterized using scanning electron micrograph (SEM), X-ray diffraction (XRD), and energy-dispersive X-ray spectroscopy (EDS) (see Supplementary Note 1). We use temperature dependent resistivity measurement and Raman spectroscopy to determine the polytype of the TaSe<sub>2</sub> samples we use in this work. 1T-TaSe<sub>2</sub> has an octahedral coordination and exhibits a normal metal to incommensurate, and incommensurate to commensurate CDW phase transition at 600 and 473 K, respectively, with the latter being associated with a sharp discontinuity in resistivity<sup>7,21,22</sup>. On the other hand, the 2H-TaSe<sub>2</sub> polytype exhibits a trigonal prismatic structure (see Fig. 1a) and remains normal metal above 123 K. Upon cooling below 123 K, it undergoes a CDW phase transition from metallic to

incommensurate phase. On further cooling, it undergoes a first order lock-in transition to commensurate 3 × 3 ordered structure around 90 K<sup>11,15</sup>. Unlike the 1T polytype, 2H-TaSe<sub>2</sub> does not exhibit any discontinuity in resistivity. The current–voltage characteristics of a 40 nm thick flake is shown in Fig. 1b at different temperatures (*T*). The normal metal to incommensurate CDW phase transition shows a sharp change in the slope in the resistivity (extracted from Fig. 1b) versus *T* plot<sup>8–10</sup>, as shown in Fig. 1c around 120 K. Above this temperature, 2H-TaSe<sub>2</sub> resistivity follows a *AT* + *B* functional form with *A* and *B* being constants, which is different from the *AT* law a conventional metal obeys. The term *B* arises from impurity scattering due to local CDW fluctuation<sup>9</sup>. Below the transition temperature *T*<sub>0</sub>, the resistivity drops as *T*<sup>2</sup> up to *T* ~ 30 K, and as *T*<sup>5</sup> for *T* < 30 K<sup>9</sup>.

2H-TaSe<sub>2</sub> exhibits conspicuous Raman active A<sub>1g</sub>, E<sub>1g</sub>, and E<sub>2g</sub> modes<sup>10,23,24</sup>, as illustrated in Fig. 1d. The A<sub>1g</sub> peak corresponds to the out of plane vibration mode at a wave number of 236 cm<sup>−1</sup>, the E<sub>2g</sub> peak corresponds to in-plane vibrational mode at 210 cm<sup>−1</sup> and a broad E<sub>1g</sub> peak at 140 cm<sup>−1</sup> results from two-phonon processes. In Supplementary Note 2, we show the X-ray photoelectron spectrum of Ta core levels (4f<sub>5/2</sub> and 4f<sub>7/2</sub>), both before and after an in situ sputter etch step. The peak positions correlate well with TaSe<sub>2</sub><sup>25</sup>. Note that, in the pre-etch measurement, while we do not observe any distinct tantalum oxide peak, after curve fitting, a higher energy peak is found which shows presence of an ultra-thin surface oxide layer. This self-limiting layer acts as a protective layer to further oxidation. We provide a detailed short-term and long-term stability analysis of the TaSe<sub>2</sub> flakes in Supplementary Note 3 using a combination of optical imaging, atomic force microscopy and Raman spectroscopy.

**Photoluminescence from metallic TaSe<sub>2</sub>.** In spite of showing metal-like conductivity behavior, the 2H-TaSe<sub>2</sub> flakes exhibit surprisingly strong PL. We acquire PL spectra from TaSe<sub>2</sub> flakes of varying thickness using continuous wave laser of wavelength 532 nm at different temperatures from 3.3 to 300 K where the sample chamber is kept at a high vacuum level of <10<sup>−7</sup> bar. The laser power is kept below 150 μW during the PL experiment. The obtained spectra from flakes of two different thickness values (monolayer and multi-layer) are shown in Fig. 2a, b. Multiple features can be readily identified in the spectra: (1) Both the films exhibit a broad prominent peak around 2.0–2.1 eV. (2) No such strong luminescence is observed when an excitation with lower energy photon (633 nm) is used. (3) The peak position blue shifts by about 30–50 meV depending on the thickness as the temperature is lowered from 300 to 3.3 K. (4) Upon cooling below 123 K, and further below 90 K, the bands of 2H-TaSe<sub>2</sub> are known to get significantly distorted to a “spaghetti-like” structure due to reconstruction<sup>11</sup>. However, we do not observe any strong signature of such reconstruction in the PL. (5) For the thick film, a weak peak is identified around 1.75 eV (indicated by red arrow in Fig. 2b), particularly at higher temperature, and this is negligible in the monolayer. Figure 2c summarizes the thickness dependence of the peak position, measured over a large number of samples at 300 K, suggesting a modulation of about 100 meV can be achieved in the emission energy by changing the thickness of the flake. It is worth noting that PL has been reported in the past from films of tantalum based compounds which have been intentionally oxidized by exposing to relatively higher power laser beam<sup>26–28</sup>. However, in our experiment, the origin of such strong PL from laser induced oxidation can be ruled out since the measurement is performed in high vacuum condition, and the laser power is also kept about an order of magnitude lower. In Supplementary Note 4, we provide a full spectrum of the PL showing the Raman lines close to the laser excitation, which

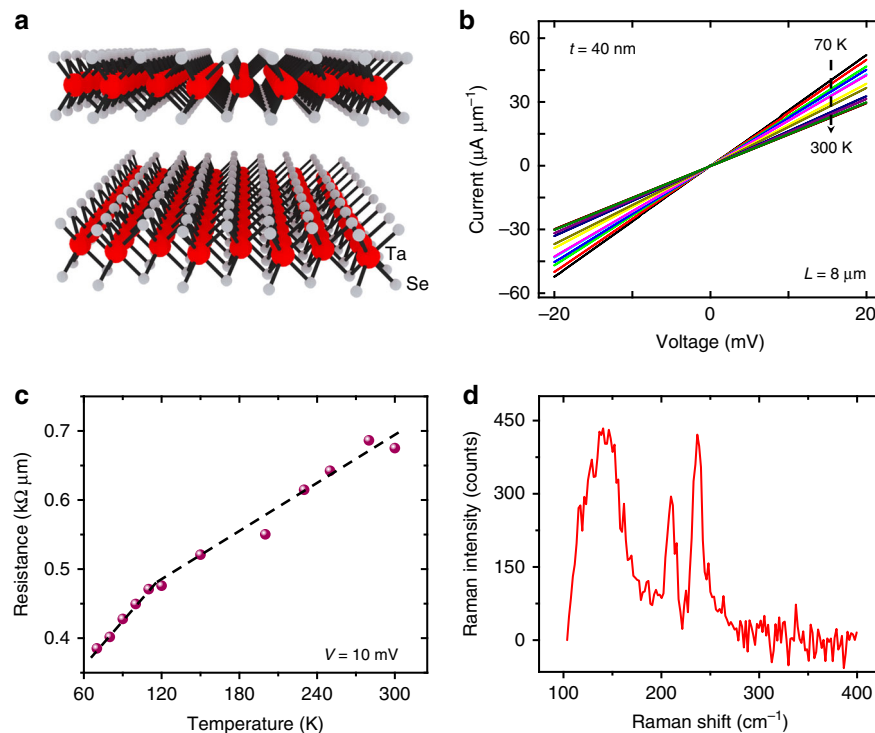


**Fig. 1** Raman and electrical characterization of 2H-TaSe<sub>2</sub>. **a** Schematic representation of crystal structure of 2H-TaSe<sub>2</sub>. **b** Current-voltage characteristics of a two-probe device using multi-layer 2H-TaSe<sub>2</sub> as the channel at different temperatures. **c** Variation of resistance (scaled by the width of the flake) with temperature as extracted from **(b)**. **d** Raman shift in multi-layer 2H-TaSe<sub>2</sub> at room temperature using a 532 nm laser

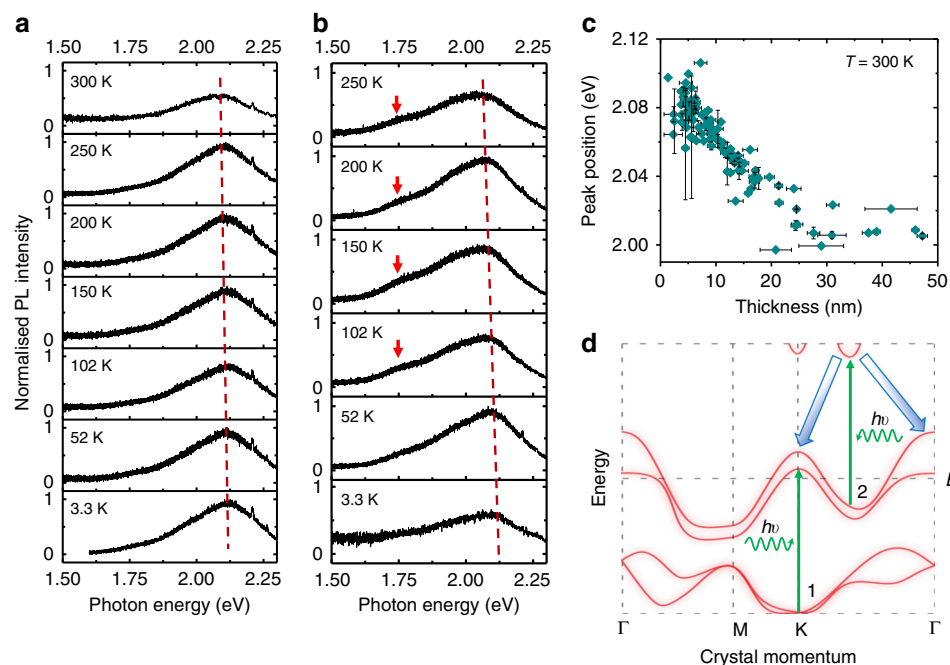


**Fig. 2** Photoluminescence (PL) from 2H-TaSe<sub>2</sub>. **a, b** Temperature dependent PL spectra of monolayer [in **(a)**] and multi-layer [in **(b)**] 2H-TaSe<sub>2</sub> flakes. **c** Variation of the PL peak position as the function of thickness. The error bars are obtained by characterizing a large number of flakes, and several measurements from different positions on each flake. **d** Schematic bandstructure of 2H-TaSe<sub>2</sub> with crystal momenta along different symmetry directions. The green arrows depict possible inter-band transitions for light absorption, while the blue arrow indicate possible inter-band carrier relaxation paths

suggests absence of any oxide Raman peak. Also, the strong dependence of the PL peak positions on the thickness of the TaSe<sub>2</sub> films clearly suggests that the observed luminescence is not resulting from any surface-oxide layer. To further establish the

point that any ambience induced surface oxidation (during exfoliation) does not give rise to the observed PL, we perform exfoliation followed by Poly(methyl methacrylate) (PMMA) spin coating inside a glovebox with N<sub>2</sub> atmosphere. The coated

samples exhibit similar PL and Raman characteristics, including a shift in the PL peak with change in flake thickness, as explained in Supplementary Note 5.

The general features of the light absorption and PL spectra can be qualitatively understood from the reported electronic structure of 2H-TaSe<sub>2</sub>, using density functional calculations<sup>12,13,24,29</sup>, tight-binding calculations<sup>11,12,30</sup>, and angle resolved photoemission spectroscopy (ARPES) measurements<sup>12,14,15,30,31</sup>. With an excitation energy of 2.33 eV, two possible direct optical transitions can be identified, as illustrated in the schematic bandstructure of a few-layer-thick 2H-TaSe<sub>2</sub> (in the normal metal state, without any reconstruction) in Fig. 2d. Like other layered CDW materials, 2H-TaSe<sub>2</sub> has a narrow band around the Fermi energy across the Brillouin zone. There are also a set of bands below and above it which are well separated in energy. Transition 1 is a direct inter-band transition from the bottom band to the band above the Fermi energy at *K* point. The photo-carriers (both electrons and holes) thus generated are scattered in the *k*-space in a very short time scale. This process is similar to gold and copper<sup>32</sup>, and results in a weak luminescence. On the other hand, transition 2 (in between  $\Gamma$  and *K*) causes a strong optical absorption due to the parallel nature of the band pair. The photo-generated electrons from the upper band relax to the *K* and  $\Gamma$  valley through indirect transitions with the assistance of phonons—resulting in luminescence.

The full width at half maximum (FWHM) of the peaks is ~250–300 meV and is significantly larger compared with typical excitonic resonance observed in monolayers of semiconducting TMDCs (like MoS<sub>2</sub>, MoSe<sub>2</sub>, WS<sub>2</sub>, and WSe<sub>2</sub>). The linewidth remains large irrespective of the thickness and sample temperature, even down to 3.3 K and can be understood from the indirect nature of carrier relaxation, as well as strong scattering from the free carriers. We also did not observe any sharp excitonic feature in differential reflectance spectra of the flakes, as shown in Supplementary Note 6.

In order to probe the lifetime of the photo-excited carriers in TaSe<sub>2</sub>, we perform time-resolved photoluminescence (TRPL) measurements. The measurement details and the results are summarized in Supplementary Note 7. Supplementary Fig. 10d shows the statistical distribution of the lifetimes extracted after deconvolving the observed data with instrument response function (IRF) across all measurements (measured over seven different flakes, several spots on each flake). The dotted curves in Supplementary Fig. 10d represent Gaussian fit to the distributions. The mean values of extracted lifetimes are 6.8 ps for 45  $\mu$ W and 2.5 ps for 140  $\mu$ W of incident power at 405 nm excitation wavelength. The distributions are found to be quite tight, with a standard deviation of 1.4 ps for 45  $\mu$ W and 0.9 ps for 140  $\mu$ W of excitation power. We, however, note that there may be some inaccuracy in these extracted lifetime values due to the closeness of the measured data with IRF. These lifetime values for the photo-carriers are significantly longer than, for example, what one would get in conventional metallic systems—a key result that is exploited later for efficient hot electron injection from TaSe<sub>2</sub> to other semiconducting TMDC.

**Resonant energy transfer between TaSe<sub>2</sub> and MoS<sub>2</sub>.** The broad emission linewidth from TaSe<sub>2</sub> has a large spectral overlap with the excitonic absorption of other semiconducting TMDC materials like A<sub>1s</sub> exciton of MoS<sub>2</sub>, as schematically shown in Fig. 3a. We exploit this feature to transfer energy from TaSe<sub>2</sub> to other semiconducting TMDC layers using dipole–dipole coupling through NRET process<sup>17–19</sup>. Due to layered structure, the transition dipoles formed in both MoS<sub>2</sub> and TaSe<sub>2</sub> are quasi-two-dimensional in nature. The dipole–dipole interaction between

these two vertically stacked materials is facilitated due to such in-plane orientation of the transition dipoles, which allow matching of the center of mass momentum<sup>33</sup>, as schematically depicted in Fig. 3b. We prepare multiple TaSe<sub>2</sub> (top)/multi-layer MoS<sub>2</sub> (bottom) vertical heterojunction stacks on Si/SiO<sub>2</sub> substrate (see “Methods”). Figure 3c shows the PL spectrum from the part of the TaSe<sub>2</sub> flake which is not on the junction. The data can be fitted with three different Voigt peaks, as shown by the dashed lines. We use a multi-layer MoS<sub>2</sub> to ensure that the luminescence from the MoS<sub>2</sub> flake alone is extremely weak. Figure 3d shows the weak MoS<sub>2</sub> peak around 1.85 eV which corresponds to the direct band gap transition at the *K*(*K'*) point of the Brillouin zone. While plotting, the MoS<sub>2</sub> peak intensity is multiplied by 5.

Figure 3e shows a sevenfold enhancement in the MoS<sub>2</sub> PL intensity (indicated by the arrow) in the TaSe<sub>2</sub>/MoS<sub>2</sub> junction. The resulting PL spectrum from the junction can now be fitted with four Voigt peaks, three from TaSe<sub>2</sub> (in dashed traces) and the fourth one representing MoS<sub>2</sub> emission (in solid black trace). At the junction, while the MoS<sub>2</sub> peak is enhanced, the individual dashed traces clearly indicate the suppression of the strength of the TaSe<sub>2</sub> emission at the emission energy of MoS<sub>2</sub>, justifying energy transfer from TaSe<sub>2</sub> to A<sub>1s</sub> exciton. The underlying mechanism is explained schematically in Fig. 3f where the rates of the individual processes are indicated. In multi-layer MoS<sub>2</sub>, the direct peak is weak due to fast (on the order of 100 fs<sup>34</sup>) transfer of carriers to lower energy indirect valleys. The photo-excited carriers generated by an excitation with 532 nm (i.e., 2.33 eV) photon—that is off-resonant with the 1 s peak—transfers to the lower valleys rather than forming an exciton in the *K* and *K'* valleys.

According to the experimental data, PL of the MoS<sub>2</sub> A<sub>1s</sub> peak gets enhanced at the MoS<sub>2</sub>/TaSe<sub>2</sub> junction suggesting a gain channel for exciton density. MoS<sub>2</sub> gains excitons at the *K* (*K'*) valley at a Forster NRET rate ( $\Gamma_{ET}^{T-M}$ ) from the energy states in TaSe<sub>2</sub> that are resonant to the exciton state of MoS<sub>2</sub>. The MoS<sub>2</sub> excitons decay through multiple parallel channels, namely the radiative recombination ( $\Gamma_r$ ) and non-radiative processes including scattering to lower energy indirect valley in MoS<sub>2</sub> ( $\Gamma_{in}$ ), as well as Dexter ( $\Gamma_{CT}^{M-T}$ ) and Forster ( $\Gamma_{ET}^{M-T}$ ) process induced exciton back transfer to TaSe<sub>2</sub>. With this understanding, we form the rate equations for exciton density in MoS<sub>2</sub> ( $N_{ex}^{M,jun}$ ) and free e-h pair density in TaSe<sub>2</sub> ( $N_{e-h}^{T,jun}$ ) on junction, as explained in Supplementary Note 8. The PL enhancement factor ( $\alpha$ ) is defined to be the ratio of the steady state PL intensity of MoS<sub>2</sub> on TaSe<sub>2</sub> to that of on SiO<sub>2</sub> and turns out to be

$$\alpha = \frac{I_M^{jun}}{I_M} = \frac{G_{e-h}^{T,jun}}{G_{ex}^M} \left\{ \frac{\Gamma_{ET}^{T-M}}{\Gamma_s \left[ 1 + \frac{\Gamma_{CT}^{M-T} + \Gamma_{ET}^{M-T}}{\Gamma_d} \right] + \Gamma_{ET}^{T-M}} \right\} \quad (1)$$

where relevant variables are defined in Supplementary Note 8. Equation (1) suggests that the enhancement factor increases as  $\Gamma_s$  decreases due to improved energy transfer with a maximum attainable value of  $\alpha_{max} = \frac{G_{e-h}^{T,jun}}{G_{ex}^M}$ . Such an efficient resonant energy transfer process is lucrative for a variety of optoelectronic applications, including electroluminescence<sup>35</sup>.

**TaSe<sub>2</sub> as an efficient hot carrier injector.** The strong light absorption by TaSe<sub>2</sub> makes it a promising material for hot carrier injection to other semiconducting materials. We fabricate MoS<sub>2</sub>/TaSe<sub>2</sub> heterojunction device with Ni/Au as contact pads, as schematically shown in Fig. 4a (see “Methods”). A laser beam of wavelength 532 nm is scanned from one contact to the other (along the arrow in the optical image in Fig. 4b), and we measure

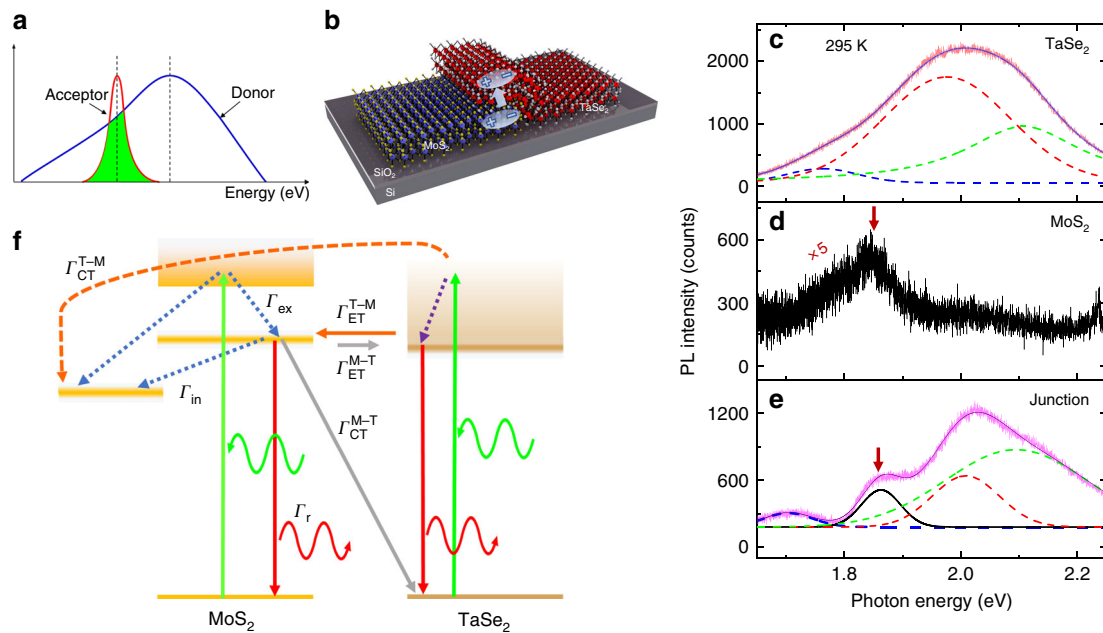


**Fig. 3** Non-radiative resonant energy transfer (NRET) between TaSe<sub>2</sub> and MoS<sub>2</sub>. **a** Schematic representation of spectral overlap required between a donor and an acceptor for NRET process. **b** Schematic representation in-plane dipole-dipole interaction between MoS<sub>2</sub> and TaSe<sub>2</sub>. **c-e** Photoluminescence (PL) spectra from **c** isolated TaSe<sub>2</sub>, **d** isolated multi-layer MoS<sub>2</sub>, and **e** MoS<sub>2</sub>/TaSe<sub>2</sub> junction at 295 K. The PL intensity from multi-layer MoS<sub>2</sub> is very weak in **(d)**, and is multiplied by 5. In **(c)**, **(e)**, the dashed traces indicate the fitted Voigt peaks from TaSe<sub>2</sub>. The fitted MoS<sub>2</sub> Voigt peak from the junction is distinct and is shown by the solid black trace in **(e)**, which suggests a seven-fold enhancement with respect to the isolated multi-layer MoS<sub>2</sub> owing to non-radiative resonant energy transfer from TaSe<sub>2</sub>. The arrow marks indicate the position of the MoS<sub>2</sub> peak in **(d-e)**. **f** Schematic representation of the different processes when the MoS<sub>2</sub>/TaSe<sub>2</sub> stack is excited with a 532 nm laser

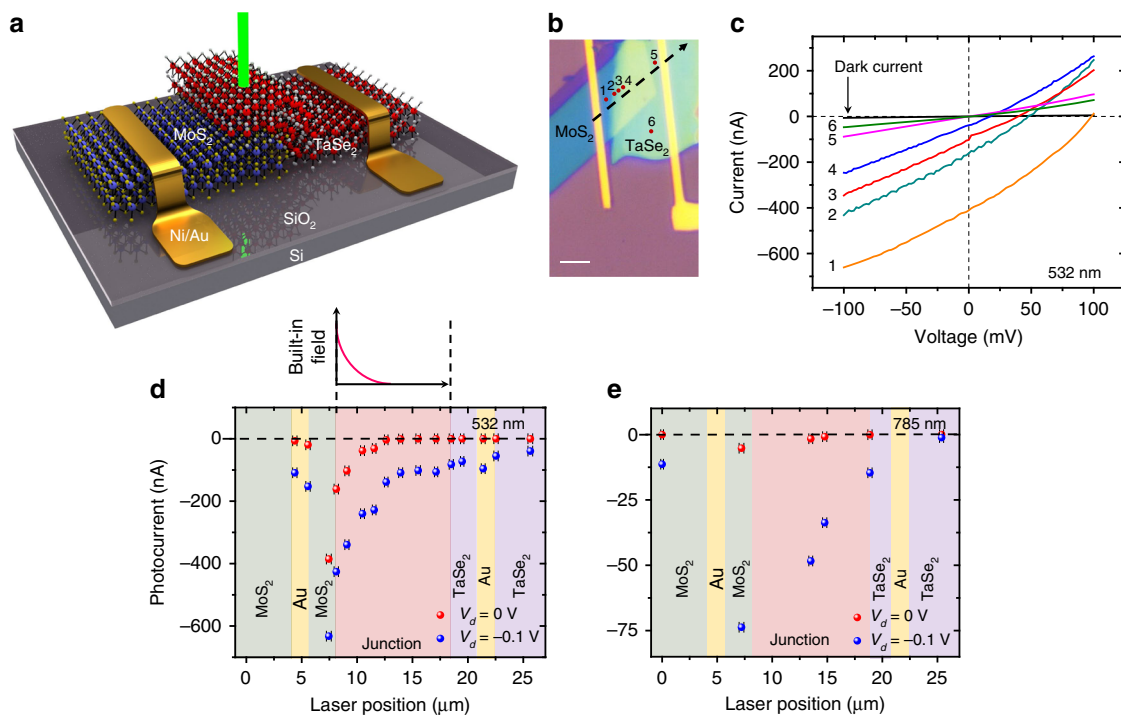


**Fig. 4** Hot Carrier injection from TaSe<sub>2</sub> to MoS<sub>2</sub>. **a** Schematic representation of the device. **b** Optical image of the fabricated heterojunction device indicating laser excitation spots (1-6) for 532 nm wavelength. The arrow indicates the direction of laser scan. Scale bar is 5 μm. **c** Current-voltage characteristics with laser spot position 1-6 as indicated in **(b)**. The dark current from the device is also shown for reference. **d, e** Spatial distribution of the photocurrent generated as a function of the laser position for an excitation wavelength of 532 nm [in **(d)**] and 785 nm [in **(e)**], at two biasing conditions, 0 V (in red spheres) and -0.1 V (in blue spheres). The error bars indicate the position accuracy of the laser spot. The top panel of **(d)** schematically shows the spatial distribution of the built-in electric field in the junction region



the corresponding photocurrent (see “Methods”) at different external bias conditions. Figure 4c shows the current–voltage characteristics of the heterojunction for a few selected positions of the laser spot, as indicated by numbers. The dark current from the device is represented by the black line. The spatial dependence of the photocurrent is illustrated in Fig. 4d at  $V_{ds} = -0.1$  V by plotting the photocurrent as a function of the laser position.

When the laser spot is on the TaSe<sub>2</sub> flake with no MoS<sub>2</sub> underneath (points 5 and 6), we observe a strong photoresponse at a non-zero external bias. This strong photocurrent away from the junction is surprising when compared to other reported metal-TMDC junction devices<sup>36</sup>. A weak photocurrent on the metal portion away from the junction has been attributed earlier to photo-thermoelectric effect due to laser spot induced local heating. However, in the present case, such a photo-thermoelectric effect can be ignored as the photocurrent strongly depends on the applied external bias, and is negligible under zero bias. This is further verified by noting that the photocurrent is extremely weak when a 785 nm excitation is used (Fig. 4e) which does not allow any inter-band transition in TaSe<sub>2</sub>. The strong photocurrent (with 532 nm) with the laser spot on TaSe<sub>2</sub> suggests that the photo-electrons, generated by the inter-band transition in TaSe<sub>2</sub>, exhibit relatively longer recombination lifetime compared to other metals. This is in good agreement with the TRPL measurement discussed earlier. The long lifetime allows us to collect the photoelectrons at the contact even when the separation between the laser spot and the metal contact is several micrometers (for example, point 6 in Fig. 4b), which is few orders of magnitude longer than conventional metals. This makes TaSe<sub>2</sub> particularly attractive material as a source for efficient hot carrier injection techniques.

When the excitation wavelength is 532 nm, the device exhibits a large open circuit voltage ( $V_{oc}$ ) and short circuit current ( $I_{sc}$ ) which strongly depend on the position of the laser spot, as explained in Fig. 4c. The asymmetry between Au/MoS<sub>2</sub> and TaSe<sub>2</sub>/MoS<sub>2</sub> junctions provides a strong built-in field in the device.  $I_{sc}$  is maximum when the laser spot is directly on the MoS<sub>2</sub> channel, and this leads to a  $V_{oc}$  of 0.1 V.  $V_{oc}$  and  $I_{sc}$  are zero on the other hand when the laser is on TaSe<sub>2</sub> as there is no built-in field in TaSe<sub>2</sub> owing to its high electrical conductivity. In between, upon moving the laser spot away from the MoS<sub>2</sub> channel towards right along the arrow in Fig. 4b, the  $V_{oc}$  and  $I_{sc}$  are gradually suppressed. Using transfer length theory<sup>37,38</sup> of metal-semiconductor contacts, the built-in field dies rapidly in the lateral direction in the MoS<sub>2</sub> portion underneath TaSe<sub>2</sub> (see top panel of Fig. 4d), resulting in a gradual suppression of the zero-bias photocurrent as the laser spot is moved away from the MoS<sub>2</sub> channel.

**Graphene/MoS<sub>2</sub>/TaSe<sub>2</sub> vertical junction.** Inspired by the strong built-in electric field in the lateral heterojunction device in Fig. 4, we next fabricate a vertical heterojunction 2H-TaSe<sub>2</sub>/2H-MoS<sub>2</sub>/1L-graphene (see “Methods”), as schematically shown in Fig. 5a. Two-dimensional layered materials have recently attracted a lot of attention as active material in photodetector applications<sup>39–41</sup>. Vertical heterojunction photodetectors based on ultra-thin two-dimensional layered materials provide a number of advantages<sup>5,42</sup> compared to lateral structures, namely (1) ultra-short carrier transit time due to nanometer separated electrodes, which is difficult to achieve otherwise in a lithography limited planar structure; (2) large built-in vertical field; (3) suppression of series resistance due to improved carrier collection efficiency that is not limited by transfer length; and (4) repeatable characteristics where encapsulated photoactive layer does not degrade from ambient effects and screened from substrate induced traps.

The difference in the work function between TaSe<sub>2</sub> and monolayer (1L) graphene provides a strong built-in field across the few-layer MoS<sub>2</sub> film which is sandwiched between the two. The structure utilizes the excellent electrical contact between TaSe<sub>2</sub> and MoS<sub>2</sub>, while maintaining the pristine nature of MoS<sub>2</sub> at the junction which is critical for the operation of such vertical heterojunction device. Monolayer graphene at the bottom serves two purposes. First, it acts like the bottom electrode for carrier collection. Second, using the weak screening through graphene, a back-gate can be used to modulate the chemical potential of the MoS<sub>2</sub> sandwiched layer.

The optical image of the fabricated heterojunction device is shown in Fig. 5b. The photocurrent ( $I_{ph}$ ) from the device is obtained as  $I_{ph} = I - I_{dark}$  where  $I$  is the measured current in presence of light and  $I_{dark}$  is the dark current. Figure 5c illustrates the variation of  $I_{ph}$  as a function of external bias when excited with a diffraction limited laser spot (diameter  $\sim 1.3$   $\mu$ m) of wavelength 532 nm. The vertical built-in field in the device manifests as a nonzero photocurrent at zero external bias. Three possible mechanisms that can contribute to the photocurrent are schematically depicted in Fig. 5d–f. The left and right panels represent the state transition diagrams and the electronic band diagrams, respectively. The first process is explained in Fig. 5d. NRET driven energy transfer due to dipole–dipole interaction between TaSe<sub>2</sub> and MoS<sub>2</sub> results in a creation of exciton in MoS<sub>2</sub> due to light absorption in TaSe<sub>2</sub>. The exciton thus created in MoS<sub>2</sub> is dissociated at a fast time scale due to scattering to lower energy indirect valleys, creating free electron and hole at the band edges. These electrons and holes are in turn separated by the built-in field, giving rise to photocurrent. Such an energy transfer driven photocurrent generation is a unique way of photodetection, and can find multiple applications in van der Waals heterojunctions. Second, the light absorbed by TaSe<sub>2</sub> creates hot electrons, which are injected into MoS<sub>2</sub>. The built-in field in MoS<sub>2</sub> carries these electrons towards graphene, resulting in photocurrent, as shown in Fig. 5e. Third, the electron–hole pairs generated by the photons directly absorbed in MoS<sub>2</sub> also result in population in the band edge indirect valleys, causing photocurrent, as explained in Fig. 5f.

In order to segregate the effect of the above three mechanisms, the photocurrent is measured with 785 nm excitation (which is not absorbed by TaSe<sub>2</sub>), and the current–voltage characteristics are summarized in the inset of Fig. 5c. We notice that the photocurrent at zero external bias is completely suppressed. This indicates that the zero-bias photocurrent for 532 nm excitation is primarily governed by TaSe<sub>2</sub> induced hot carrier transfer and dipole–dipole interaction driven NRET process.

The photocurrent is plotted as a function of the incident optical power ( $P_{op}$ ) of 532 nm excitation in Fig. 6a. The data can be fitted with a power law:  $I_{ph} \propto P_{op}^{0.52}$ , which indicates that the traps due to the gap states in MoS<sub>2</sub> play an important role in determining  $I_{ph}$ . The presence of gap states in MoS<sub>2</sub> (see Fig. 6b) is also identified by the back gate modulation of the electrical conductivity of the device. Figure 6c shows the transfer characteristics [drain current ( $I_d$ ) versus gate voltage ( $V_g$ )] where  $V_g$  is applied at the back side. Upon cooling the device to 77 K, we obtain an on-off ratio of  $\sim 6.6 \times 10^3$ , which reduces to  $\sim 45$  at 280 K. The on-off ratio at 280 K suffers from tunneling of carriers from bottom graphene electrode to top TaSe<sub>2</sub> electrode though the bandgap states in MoS<sub>2</sub> resulting from band tail states as well as deep traps due to defects<sup>43</sup>. The tunneling effect manifests in a particularly strong manner for large negative  $V_g$ , where the gate voltage dependence on the drain current is completely absent due to the tunneling leakage. When the device is cooled down to 77 K, the trap assisted tunneling can be reduced significantly. The

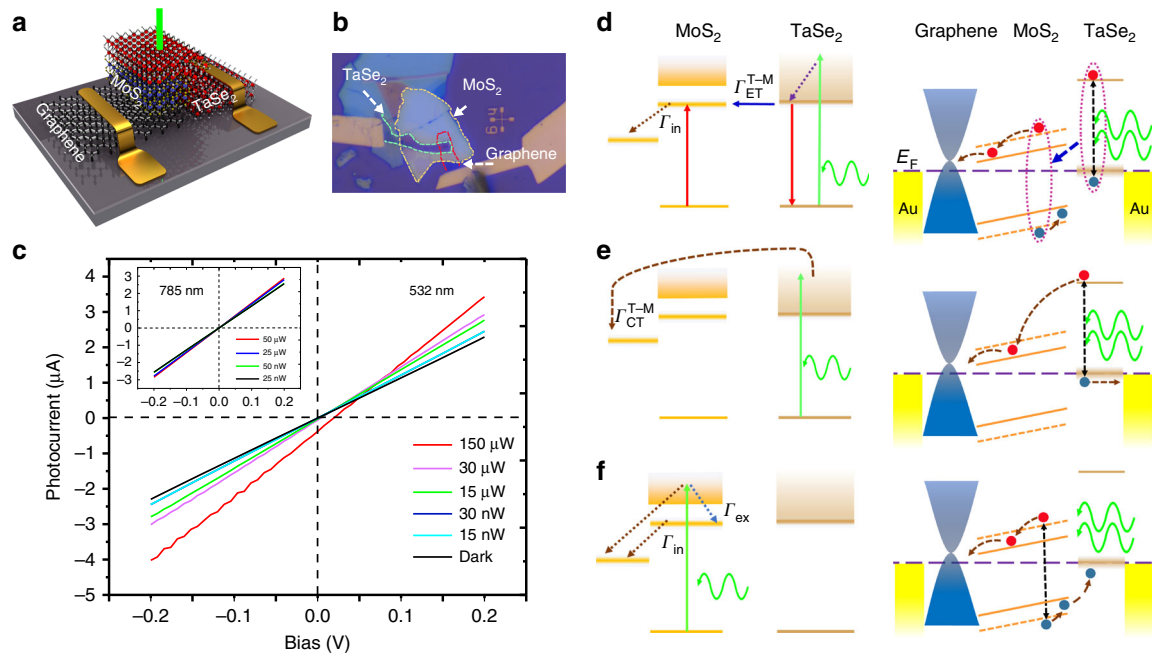


**Fig. 5** Photocurrent generation mechanism in TaSe<sub>2</sub>/MoS<sub>2</sub>/graphene vertical heterojunction. **a, b** Schematic diagram and optical micrograph of the device. **c** Current-voltage characteristics of the device with various incident power of 532 nm laser. Inset: Current-voltage characteristics with 785 nm laser at different incident powers. **d, e, f** Schematic representation various photocurrent generation mechanisms in the heterojunction. The left panels represent transition diagrams and the right panels indicate the corresponding process in the electronic band diagram. The mechanism in **(d)** is governed by absorption in TaSe<sub>2</sub> followed by energy transfer in MoS<sub>2</sub> and subsequent dissociation of exciton to lower energy indirect valleys. In **(e)**, light is absorbed by TaSe<sub>2</sub> followed by hot carrier transfer to indirect valley in MoS<sub>2</sub>. In **(f)**, the mechanism is governed by direct absorption in MoS<sub>2</sub>.

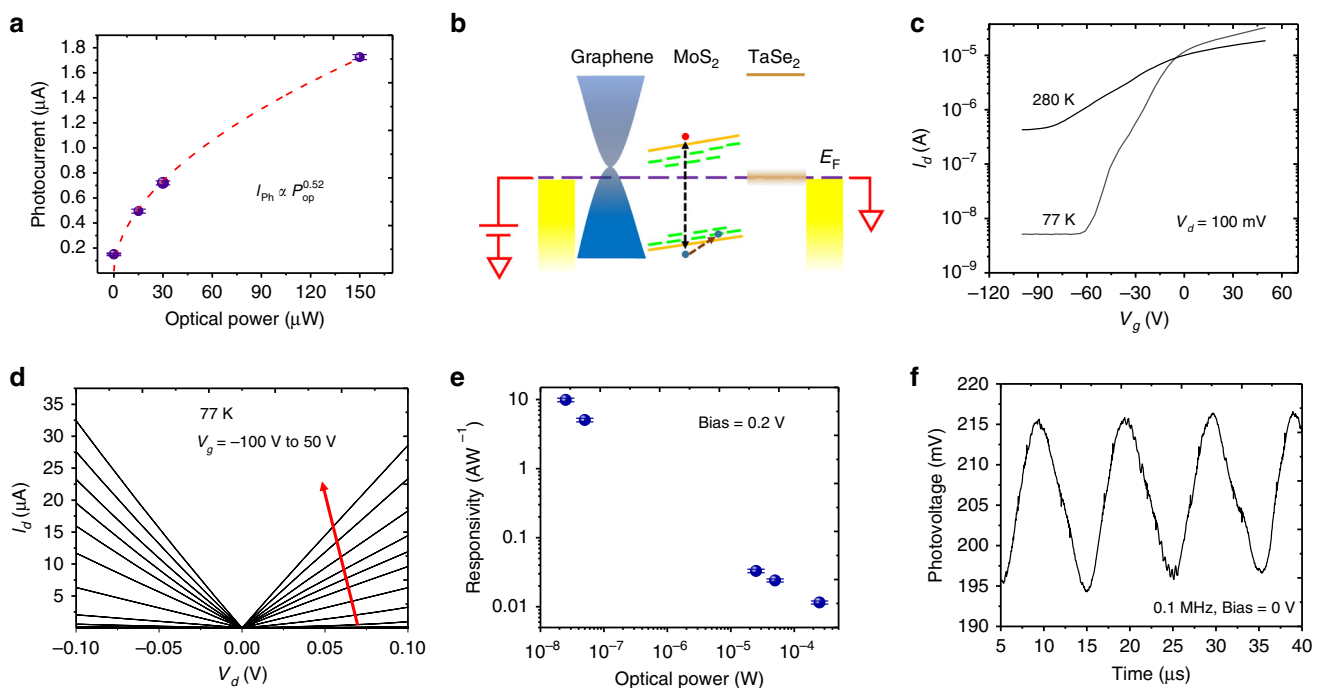


**Fig. 6** Performance of TaSe<sub>2</sub>/MoS<sub>2</sub>/graphene photodetector. **a** Photocurrent as a function of incident optical power for 532 nm wavelength. Exponent in the power law fitting is 0.52, showing the role of traps in the device performance. The error bars are obtained from multiple measurements. **b** Schematic illustration of hole trapping in the existing gap states in MoS<sub>2</sub>. **c** Transfer characteristics ( $I_d$  versus  $V_g$ ) of a vertical device at both 77 K and 280 K. Leakage current in the OFF state increases with temperature, indicating trap assisted tunneling through the bandgap of MoS<sub>2</sub>. **d** Output characteristics ( $I_d$  versus  $V_d$ ) of vertical device at 77 K. Gate bias is varied from -100 V to 50 V. **e** Variation of responsivity with incident optical power at a wavelength of 532 nm. Device is biased at 200 mV. The error bars are obtained from multiple measurements. **f** Transient photoresponse of the device measured at zero external bias when the light intensity is modulated at 0.1 MHz.

output characteristics [ $I_d$  versus drain voltage ( $V_d$ )] of the vertical device at 77 K are displayed in Fig. 6d.

Figure 6e shows the obtained responsivity ( $R = \frac{I_{ph}}{P_{op}}$ ) from the device at different incident optical powers. The responsivity is  $>10$  at the minimum power used, which suggests an internal gain in the device. The different photo-carrier generation mechanisms described earlier also populate the trap states closer to the valence band of  $\text{MoS}_2$  with holes. This in turn results in a gain mechanism<sup>42,43</sup>. Two possible mechanisms, namely photoconductive gain and photogating effect, provide gain in the system. Photo-generated holes trapped in the gap states of the  $\text{MoS}_2$  film cause a charge imbalance forcing reinjection of electrons multiple times before the trapped hole recombines or tunnels out of  $\text{MoS}_2$ —providing photoconductive gain. Electron trapping is neglected as the Fermi level in  $\text{MoS}_2$  lies close to the conduction band edge. Since the photoconductive gain is given by  $\frac{\tau}{\tau_{tr}}$ , where  $\tau$  is the lifetime of the hole in the trap state, the vertical structure is advantageous due to its short transit time ( $\tau_{tr}$ ) of electrons through the thin  $\text{MoS}_2$  layer<sup>5</sup>. On the other hand, the trapped holes suppress the barrier for carrier injection to  $\text{MoS}_2$  from vertical electrodes, providing a photogating effect.

The heterostructure device is further characterized for the speed of operation using a laser which is intensity modulated with varying frequency. The photovoltage generated by the device is measured across a digital storage oscilloscope which is terminated with 10 M $\Omega$  impedance. Figure 6f shows the measured photovoltage in response to a 0.1 MHz modulation frequency under zero external bias operation, which is one of the fastest reported photodetectors using TMDC material. The short transit time of the photo-electrons helps to obtain the high speed of operation of the detector, while maintaining the gain. In Supplementary Table 1, we compare the performance of the photodetector presented in this work with existing 2D material based detectors (having response time less than 100 ms).

## Discussion

In summary, we demonstrate the versatility of 2H-TaSe<sub>2</sub> as a two-dimensional layered CDW material, which exhibits metal-like characteristics, coupled with strong light absorption and emission due to energy separated bands. The narrow band around the Fermi energy results in giant metallic conductivity with temperature dependent CDW characteristics. This makes TaSe<sub>2</sub> an ideal candidate for a 2D-2D van der Waals contact material which can maintain the pristine nature of the underneath 2D layered semiconductor. On the other hand, the well separated bands lying above and below the Fermi energy result in strong inter-band optical absorption, strong PL and a long lifetime of photoelectrons generating large photocurrent. The spectral overlap between emission of TaSe<sub>2</sub> and excitonic absorption of other TMDC semiconductors like  $\text{MoS}_2$  results in a unique in-plane momentum matched 2D-2D combination of donor-acceptor pair causing a giant enhancement of PL in multi-layer  $\text{MoS}_2$  due to NRET. TaSe<sub>2</sub> is further utilized as a dual-purpose layer in a vertical photodetection device to obtain high speed and gain simultaneously. The large separation of the bands also make TaSe<sub>2</sub> an interesting material for low-loss plasmonic applications<sup>44,45</sup>. The finding will ignite multiple device applications using 2H-TaSe<sub>2</sub> in the nano-opto-electronic domain.

## Methods

**Heterojunction device fabrication.** For both planar and vertical devices, the 2D material stack is fabricated by using dry transfer technique on a highly doped Si substrate coated with 285 nm thick thermally grown oxide. This stack is heated on a hot plate at 80 °C for 2 min for improved adhesion between layers. Devices are fabricated using standard nano-fabrication methods. The substrate is spin coated

with PMMA 950C3 and baked on a hot plate at 180 °C for 2 min. This is followed by electron beam lithography with an acceleration voltage of 20 KV, an electron beam current of 300 pA, and an electron beam dose of 200  $\mu\text{Ccm}^{-2}$ . Patterns were developed using MIBK:IPA solution in the ratio 1:3. Later samples are washed in isopropyl alcohol and dried in  $\text{N}_2$  blow. 10 nm Ni/50 nm Au films are deposited by using magnetron sputtering with the help of Ar plasma at  $3 \times 10^{-3}$  mBar. Metal lift-off was done by dipping the substrate in acetone for 15 min, followed by washing in isopropyl alcohol and  $\text{N}_2$  drying. The bottom side of the wafer is etched by dilute HF solution and silver film is deposited as the bottom gate contact.

**Photocurrent measurements.** Devices are probed by micromanipulators, connected to a Keithley 2636B and Agilent B1500 device analyzers for electrical measurements. Diffraction limited laser spots of wavelength 532 nm and 785 nm are used for photocurrent measurements through a  $\times 50$  objective with a numerical aperture of 0.5. The device is kept on a motorized stage to obtain spatial mapping of photocurrent. For low temperature electrical measurements, a liquid nitrogen cooled stage is used. High speed measurements are performed using a 532 nm laser beam. The intensity of the laser beam is modulated at the required frequency, up to 0.1 MHz and the photovoltage measured using a digital storage oscilloscope which is terminated by 10 M $\Omega$ .

## Data availability

The datasets generated and analyzed during the current study are available from the corresponding author on reasonable request.

Received: 18 April 2019 Accepted: 4 July 2019

Published online: 31 July 2019

## References

- Lee, C. H. et al. Atomically thin p–n junctions with van der waals heterointerfaces. *Nat. Nanotechnol.* **9**, 676 (2014).
- Withers, F. et al. WSe<sub>2</sub> light-emitting tunneling transistors with enhanced brightness at room temperature. *Nano Lett.* **15**, 8223–8228 (2015).
- Shim, J. et al. Electronic and optoelectronic devices based on two-dimensional materials: From fabrication to application. *Adv. Electron. Mater.* **3**, 1600364 (2017).
- Massicotte, M. et al. Picosecond photoresponse in van der waals heterostructures. *Nat. Nanotechnol.* **11**, 42–46 (2016).
- Kallatt, S., Nair, S. & Majumdar, K. Asymmetrically encapsulated vertical ITO/ $\text{MoS}_2$ / $\text{Cu}_2\text{O}$  photodetector with ultrahigh sensitivity. *Small* **14**, 1702066 (2018).
- Withers, F. et al. Light-emitting diodes by band-structure engineering in van der waals heterostructures. *Nat. Mater.* **14**, 301 (2015).
- Wilson, J. A., Di Salvo, F. J. & Mahajan, S. Charge-density waves in metallic, layered, transition-metal dichalcogenides. *Phys. Rev. Lett.* **32**, 882 (1974).
- Lee, H., Garcia, M., McKinzie, H. & Wold, A. The low-temperature electrical and magnetic properties of TaSe<sub>2</sub> and NbSe<sub>2</sub>. *J. Solid State Chem.* **1**, 190–194 (1970).
- Naito, M. & Tanaka, S. Electrical transport properties in 2H-NbSe<sub>2</sub>, -NbSe<sub>2</sub>, -TaSe<sub>2</sub> and -TaSe<sub>2</sub>. *J. Phys. Soc. Jpn.* **51**, 219–227 (1982).
- Neal, A. T., Du, Y., Liu, H. & Ye, P. D. Two-dimensional TaSe<sub>2</sub> metallic crystals: spin–orbit scattering length and breakdown current density. *ACS Nano* **8**, 9137–9142 (2014).
- Rossnagel, K. & Smith, N. V. Spin-orbit splitting, fermi surface topology, and charge-density-wave gapping in 2H-TaSe<sub>2</sub>. *Phys. Rev. B* **76**, 073102 (2007).
- Laverock, J. et al. k-resolved susceptibility function of 2H-TaSe<sub>2</sub> from angle-resolved photoemission. *Phys. Rev. B* **88**, 035108 (2013).
- Renteria, J. et al. All-metallic electrically gated 2H-TaSe<sub>2</sub> thin-film switches and logic circuits. *J. Appl. Phys.* **115**, 034305 (2014).
- Tsoutsou, D. et al. Epitaxial 2d  $\text{MoSe}_2$  ( $\text{HfSe}_2$ ) semiconductor/2D TaSe<sub>2</sub> metal van der waals heterostructures. *ACS Appl. Mater. Interfaces* **8**, 1836–1841 (2016).
- Li, Y. W. et al. Folded superstructure and degeneracy-enhanced band gap in the weak-coupling charge density wave system 2H-TaSe<sub>2</sub>. *Phys. Rev. B* **97**, 115118 (2018).
- Shi, J. et al. Chemical vapor deposition grown wafer-scale 2D Tantalum Diselenide with robust charge-density-wave order. *Adv. Mater.* **30**, 1804616 (2018).
- Kozawa, D. et al. Evidence for fast interlayer energy transfer in  $\text{MoSe}_2$ /WS<sub>2</sub> heterostructures. *Nano Lett.* **16**, 4087–4093 (2016).
- Guzelturk, B. & Demir, H. V. Near-field energy transfer using nanoemitters for optoelectronics. *Adv. Funct. Mater.* **26**, 8158–8177 (2016).
- Deshmukh, R. et al. Long-range resonant energy transfer using optical topological transitions in metamaterials. *ACS Photonics* **5**, 2737–2741 (2018).



20. Dandu, M. et al. Strong single- and two-photon luminescence enhancement by non-radiative energy transfer across layered heterostructure. *ACS Nano* **13**, 4795–4803 (2019).
21. Wilson, J. A., Di Salvo, F. J. & Mahajan, S. Charge-density waves and superlattices in the metallic layered transition metal dichalcogenides. *Adv. Phys.* **24**, 117–201 (1975).
22. Inada, R., Onuki, Y. & Tanuma, S. Hall effect of 1T-TaS<sub>2</sub> and 1T-TaSe<sub>2</sub>. *Phys. B + C* **99**, 188–192 (1980).
23. Hajiyev, P., Cong, C., Qiu, C. & Yu, T. Contrast and Raman spectroscopy study of single- and few-layered charge density wave material: 2H-TaSe<sub>2</sub>. *Sci. Rep.* **3**, 2593 (2013).
24. Yan, J. A., Cruz, M. A. D., Cook, B. & Varga, K. Structural, electronic and vibrational properties of few-layer 2H- and 1T-TaSe<sub>2</sub>. *Sci. Rep.* **5**, 16646 (2015).
25. Luo, H. et al. Differences in chemical doping matter: Superconductivity in Ti<sub>1-x</sub>Ta<sub>x</sub>Se<sub>2</sub> but not in Ti<sub>1-x</sub>Nb<sub>x</sub>Se<sub>2</sub>. *Chem. Mater.* **28**, 1927–1935 (2016).
26. Castellanos-Gomez, A. et al. Fast and reliable identification of atomically thin layers of TaSe<sub>2</sub> crystals. *Nano Res.* **6**, 191–199 (2013).
27. Coronado, E., Forment-Aliaga, A., Navarro-Moratalla, E., Pinilla-Cienfuegos, E. & Castellanos-Gomez, A. Nanofabrication of TaS<sub>2</sub> conducting layers nanopatterned with Ta<sub>2</sub>O<sub>5</sub> insulating regions via AFM. *J. Mater. Chem. C* **1**, 7692–7694 (2013).
28. Cartamil-Bueno, S. J. et al. High-quality-factor tantalum oxide nanomechanical resonators by laser oxidation of TaSe<sub>2</sub>. *Nano Res.* **8**, 2842–2849 (2015).
29. Kuchinskii, E. Z., Nekrasov, I. A. & Sadovskii, M. V. Electronic structure of two-dimensional hexagonal diselenides: charge density waves and pseudogap behavior. *J. Exp. Theor. Phys.* **114**, 671–680 (2012).
30. Smith, N. V., Kevan, S. D. & Di Salvo, F. J. Band structures of the layer compounds 1T-TaS<sub>2</sub> and 2H-TaSe<sub>2</sub> in the presence of commensurate charge-density waves. *J. Phys. C: Solid State Phys.* **18**, 3175 (1985).
31. Jakovidis, G., Riley, J. D. & Leckey, R. C. G. Experimental bandstructure of 2H-TaSe<sub>2</sub>. *J. Electron Spectrosc. Relat. Phenom.* **61**, 19–26 (1992).
32. Mooradian, A. Photoluminescence of metals. *Phys. Rev. Lett.* **22**, 185 (1969).
33. Lyo, S. K. Energy transfer of excitons between quantum wells separated by a wide barrier. *Phys. Rev. B - Condens. Matter Mater. Phys.* **62**, 13641–13656 (2000).
34. Bertoni, R. et al. Generation and evolution of spin-, valley-, and layer-polarized excited carriers in inversion-symmetric WSe<sub>2</sub>. *Phys. Rev. Lett.* **117**, 277201 (2016).
35. Puchert, R. P. et al. Spectral focusing of broadband silver electroluminescence in nanoscopic fret-leds. *Nat. Nanotechnol.* **12**, 637 (2017).
36. Hong, T. et al. Plasmonic hot electron induced photocurrent response at MoS<sub>2</sub>-metal junctions. *ACS Nano* **9**, 5357–5363 (2015).
37. Schroder, D. K. *Semiconductor Material and Device Characterization*. (Wiley-Interscience, Hoboken, New Jersey, 2006).
38. Majumdar, K. et al. STLM: a sidewall tlm structure for accurate extraction of ultralow specific contact resistivity. *IEEE Electron Device Lett.* **34**, 1082–1084 (2013).
39. Koppens, F. H. L. et al. Photodetectors based on graphene, other two-dimensional materials and hybrid systems. *Nat. Nanotechnol.* **9**, 780 (2014).
40. Li, X. et al. Graphene and related two-dimensional materials: structure-property relationships for electronics and optoelectronics. *Appl. Phys. Rev.* **4**, 021306 (2017).
41. Mak, K. F. & Shan, J. Photonics and optoelectronics of 2D semiconductor transition metal dichalcogenides. *Nat. Photonics* **10**, 216 (2016).
42. Murali, K. & Majumdar, K. Self-powered, highly sensitive, high-speed photodetection using ITO/WSe<sub>2</sub>/SnSe<sub>2</sub> vertical heterojunction. *IEEE Trans. Electron Devices* **65**, 4141–4148 (2018).
43. Furchi, M. M., Polyushkin, D. K., Pospischil, A. & Mueller, T. Mechanisms of photoconductivity in atomically thin MoS<sub>2</sub>. *Nano Lett.* **14**, 6165–6170 (2014).
44. Khurgin, J. B. & Sun, G. In search of the elusive lossless metal. *Appl. Phys. Lett.* **96**, 181102 (2010).
45. Gjerding, M. N., Pandey, M. & Thygesen, K. S. Band structure engineered layered metals for low-loss plasmonics. *Nat. Commun.* **8**, 15133 (2017).

## Acknowledgements

This work was partially supported in part by a grant under Indian Space Research Organization (ISRO), by the grants under Ramanujan Fellowship, Early Career Award, and Nano Mission from the Department of Science and Technology (DST), and by a grant from MHRD, MeitY and DST Nano Mission through NNetRA. S.G. acknowledges funding support from DST (SR/FST/ETII-072/2016) and SERB (SB/S2/RJN-134/2014, EMR/2016/007113).

## Author contributions

K.M. designed the experiment. M.M. and S.K. prepared the samples, fabricated the devices and performed the measurements. N.S. and S.G. performed the time-resolved photoluminescence measurement. M.D. contributed to the theoretical analysis of the energy transfer mechanism. All authors contributed to the data analysis, discussion of results, and writing of the paper. M.M. and S.K. contributed equally to this work.

## Additional information

**Supplementary information** accompanies this paper at <https://doi.org/10.1038/s42005-019-0190-0>.

**Competing interests:** The authors declare no competing interests.

**Reprints and permission** information is available online at <http://npg.nature.com/reprintsandpermissions/>

**Publisher's note:** Springer Nature remains neutral with regard to jurisdictional claims in published maps and institutional affiliations.



**Open Access** This article is licensed under a Creative Commons Attribution 4.0 International License, which permits use, sharing, adaptation, distribution and reproduction in any medium or format, as long as you give appropriate credit to the original author(s) and the source, provide a link to the Creative Commons license, and indicate if changes were made. The images or other third party material in this article are included in the article's Creative Commons license, unless indicated otherwise in a credit line to the material. If material is not included in the article's Creative Commons license and your intended use is not permitted by statutory regulation or exceeds the permitted use, you will need to obtain permission directly from the copyright holder. To view a copy of this license, visit <http://creativecommons.org/licenses/by/4.0/>.

© The Author(s) 2019